nature nanotechnology

SUPPLEMENTARY INFORMATION

DOI: 10.1038/NNANO.2016.268

In the format provided by the authors and unedited.

Targeted intracellular voltage recordings from dendritic spines using quantum-dot-coated nanopipettes

Krishna Jayant, Jan J. Hirtz, Ilan Jen-La Plante, David M. Tsai,Wieteke D.A.M De Boer, Alexa Semonche, Darcy S. Peterka, Jonathan S. Owen, Ozgur Sahin, Kenneth L. Shepard and Rafael Yuste

To whom correspondence should be addressed: Krishna Jayant; email:kj2346@columbia.edu

This file includes:

© 2016 Macmillan Publishers Limited, part of Springer Nature. All rights reserved.

Supplementary Note1: quantum-dot characteristics and preparation

Single photon absorption and fluorescence spectra were recorded with a Perkin-Elmer (WA, Massachusetts, USA) Lambda 650 scanning UV-Vis spectrophotometer and a HORIBA Jobin Yvon (Edison, NJ, USA) Fluoromax 4 fluorometer, respectively (**Supplementary Fig. 1(a)**). Two photon absorption spectra (**Supplementary Fig. 1(b))** was carried out as follows: The QD fluorescence was collected with an Ocean Optics USB2000 spectrometer coupled to the microscope setup with an optical fiber. The spectrum (red – left y-axis) was recorded with excitation wavelength at λ_{exc} = 800 nm (collection time t_{coll} = 10 ms), and is consistent with the 1P excited emission spectrum shown in **Supplementary Fig. 1(a)**. The 2P absorption profile (black dots – right y-axis) was recorded for the wavelength regime between λ = 800 – 1100 nm as to confirm the 2P intensity dependence. The intensity profile was constructed from the images recorded with a photomultiplier tube.

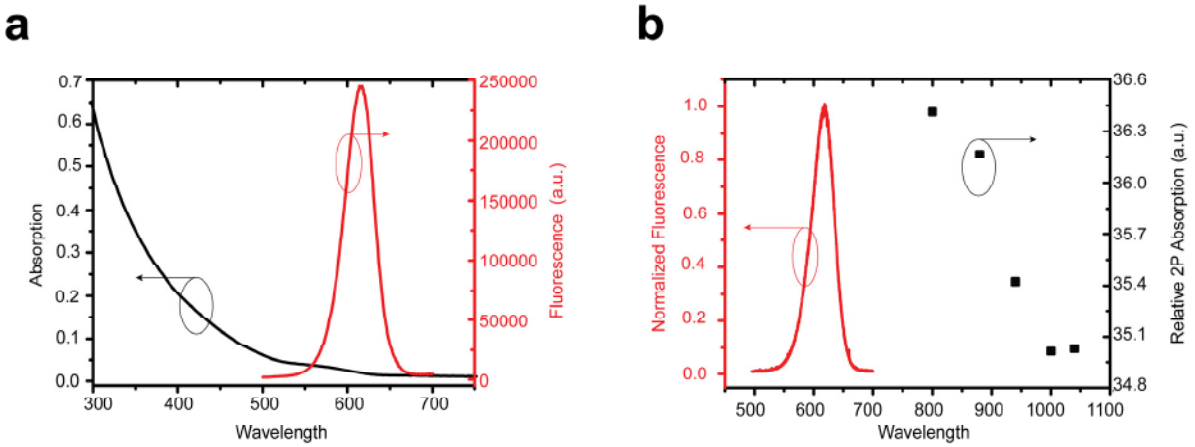

Supplementary Figure 1: QD absorption spectra a, Single photon absorption (left y-axis) and fluorescence spectra (right axis) of CdSe/CdS/ZnS QDs dispersed in hexane plotted between λ = 300 – 750 nm. The onset of the absorption is around λ = 600 nm and steadily increases toward shorter wavelengths. The emission peak, recorded with excitation λ = 400 nm, is centered around λ = 615 nm and has a FWHM of ~40 nm. The fluorescence quantum efficiency was determined for excitations λ = 400 nm and λ = 470 nm and found to be QE = 11%, and QE = 14.5%, respectively. **b,** The 2P excited fluorescence spectrum (left) and 2P absorption profile (right) for hexane-dissolved CdSe/CdS/ZnS QDs deposited on a quartz pipette, plotted between λ = 450 – 1100 nm.

We assumed that the internal fluorescence quantum efficiency of the QD was independent of the excitation conditions, rendering the 2P absorption cross section the only variable. The excitation

© 2016 Macmillan Publishers Limited, part of Springer Nature. All rights reserved.

power was kept constant throughout the entire wavelength regime and set to low values, in order to avoid possible saturation effects for QD light absorption (verified by a linear dependence found for three different excitation powers – not shown). Detection conditions (i.e. photomultiplier collection time and sensitivity gain) for this experiment were kept constant for all excitation wavelengths, so that only background correction of the emission signal was required – it should be noted that any changes in the beam profile and pulse width have been assumed to be negligibly small for this wavelength regime. The spectral profile follows a similar trend as the 1P absorption spectrum shown in **Supplementary Fig. 1(a)**. At double the wavelength: for the shorter wavelength regime the absorption intensity is the highest with a gradual decrease toward longer wavelengths. It is evident from the 2P absorption profile that (λ_{exc} = 940 nm, used in this study) the excitation condition is not the most optimal for efficient excitation of the QDs but provides enough luminescence to allow dual color readout (Alexa 488 and QD).

- *METHOD: QD preparation*

CdSe/CdS/ZnS nanocrystals were prepared by first forming CdSe and then adding CdS and ZnS shell layers. First, wurtzite CdSe nanocrystals were synthesized as previously described with slight modifications[1]. Briefly, cadmium oxide (77 mg, 0.6 mmol) and oleic acid (0.68 g, 2.4 mmol) were added to 1-octadecene (6.0 g), degassed under Ar flow (30 min), then heated to 240 °C until clear (15 minutes). This solution was then cooled to <70 °C and trioctylphosphine (1.5 g) and octadecylamine (4.5 g) were added under an overpressure of Ar. The reaction solution was then heated to 270 °C and 3.0 g of tributylphosphine selenide diluted in 1-octadecene (Se, 1.4 g, 17.6 mmol; tributylphosphine, 3.84 g, 18.8 mmol; 1-octadecene, 12.3 g) was injected rapidly and the temperature reduced to 250 °C. The reaction is allowed to proceed for three minutes (resulting in nanocrystals with a 3.6 nm diameter), cooled to <80 °C, and diluted with hexane (10 mL). The hexane solution was washed twice with methanol before proceeding.

CdS and ZnS shells were grown on the preformed CdSe cores using an alternating addition strategy described elsewhere[2]. CdSe cores dissolved in hexane (100 nmol in QDs) were added to octadecylamine (1.5 g) and 1-octadecene (5.0 g) and degassed under vacuum to remove all hexane (30 minutes, 100 °C). The reaction solution was then heated to 240 °C under Ar. Next, alternating additions of cadmium oleate (0.04 M in 1-octadecene; CdO, 62 mg, 0.48 mmol; oleic

© 2016 Macmillan Publishers Limited, part of Springer Nature. All rights reserved.

acid, 1.08 g, 3.83 mmol; 1-octadecene, 8.5 g) and N-n-hexyl-N'-di-n-octylthiourea (0.04 M in 1-octadecene; N-n-hexyl-N',N'-di-n-octylthiourea, 154 mg, 0.4 mmol; 1-octadecene, 7.9 g) were added dropwise to the reaction for the formation of CdS layers. Following the growth of CdS, alternating additions of zinc oleate (0.04 M in 1-octadecene; zinc acetate dihydrate, 44 mg, 0.20 mmol; oleic acid, 0.24 g, 0.85 mmol; 1-octadecene, 6.0 g) and N-n-hexyl-N',N'-di-n-octylthiourea (0.04 M in 1-octadecene) were added dropwise for the formation of the ZnS layers. Following each addition, the mixture was allowed to react for 10 minutes. After the last addition, the solution was cooled to <80 °C and toluene was added (10 mL). Sufficient methyl acetate was added to form a cloudy suspension (approximately 10 mL), which was then centrifuged. The solid nanocrystal residue was dissolved in toluene and stored in the dark.

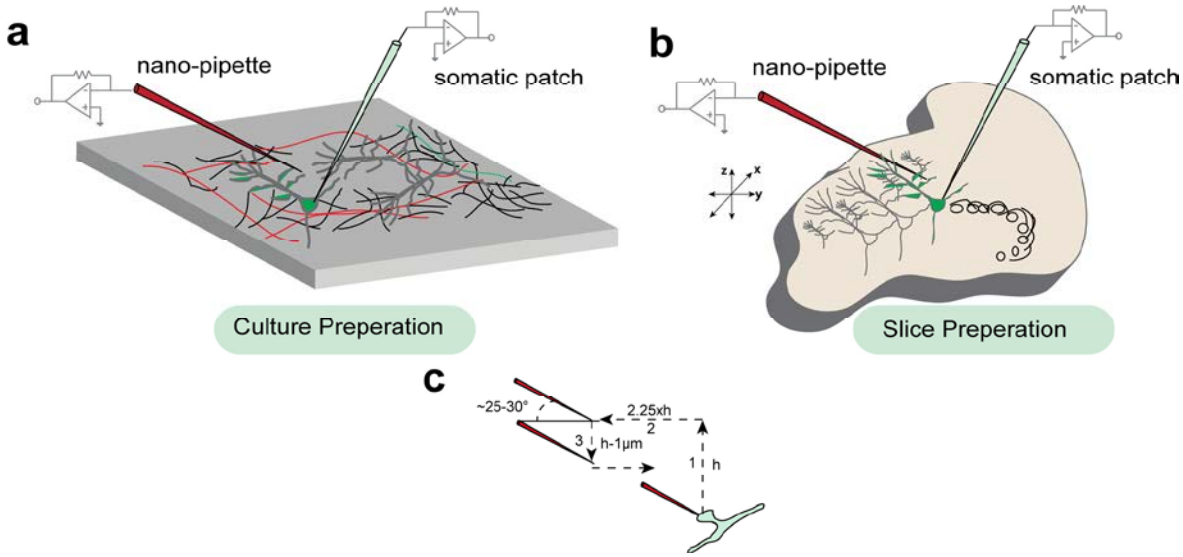

Supplementary Figure 2:Experimental approach a, schematic representation of dual somato-spine recordings in cultures and **b,** slices. **c,** nanopipette navigation approach in slices towards a chosen target

© 2016 Macmillan Publishers Limited, part of Springer Nature. All rights reserved.

Supplementary Note2: Transient response and deconvolution

➢ *Equivalent circuit transient response:*

Using Kirchhoff's law's and solving for the transient response for the circuit[3] shown in **Supplementary Fig. 3(a)** (corresponds to model A in main manuscript) , we arrive at the following expression;

$$\tau_m\tau_e\frac{d^2V_p}{dt^2}+(\tau_m+\tau_e+\tau_c+\tau_e\frac{R_m}{R_{shunt}})\frac{dV_p}{dt}+V_p(\frac{R_{shunt}+R_m}{R_{shunt}})=\frac{R_mV_d+E_{rest}R_{shunt}}{R_{shunt}} \quad (1)$$

Here, $\tau_m=R_mC_m$, $\tau_e=R_eC_e$ and $\tau_c=R_mC_e$. At steady state (i.e. at t=0) , the RMP reduces to

$$V_p=E_{steady\_state}=\frac{R_mV_d+E_{rest}R_{shunt}}{R_{shunt}+R_m} \quad (2)$$

The diffusion potential can be approximated to zero (i.e. bath is grounded for all practical purposes), which gives us the general expression for the steady state RMP;

$$V_p=E_{steady\_state}=\frac{E_{rest}R_{shunt}}{R_{shunt}+R_m} \quad (3)$$

It is important to note that the amplifier is considered to have a very high input impedance and hence no current flows into the amplifier. For model B (**Supplementary Fig. 3(b)**) a similar expression for the steady state RMP is arrived at with minor differences (Eq. 4(a&b) and with $V_d=0$) and $\tau_d=R_pC_e$. Here, the RMP is decided by the magnitude of the R_{pore} and R_{seal}. Interestingly, if R_{pore} is negligible , the expression is similar to Eq. (3) with $V_d=0$. Hence Eq.4b represents distributed shunting (i.e. across the pore and seal).

$$(\tau_m\tau_e+\tau_m\tau_e\frac{R_{pore}}{R_{seal}}+\tau_m\tau_d)\frac{d^2V_p}{dt^2}+(\tau_m+\tau_d+\tau_c+\tau_e(1+\frac{R_{pore}}{R_{seal}}+\frac{R_m}{R_{seal}})\frac{dV_p}{dt}.....$$

$$.....+V_p(1+\frac{R_m}{R_{seal}}+\frac{R_{pore}}{R_{seal}})=E_{rest} \quad (4a)$$

$$V_p=E_{steady\_state}=\frac{E_{rest}R_{seal}}{R_{seal}+R_{pore}+R_m} \quad (4b)$$

© 2016 Macmillan Publishers Limited, part of Springer Nature. All rights reserved.

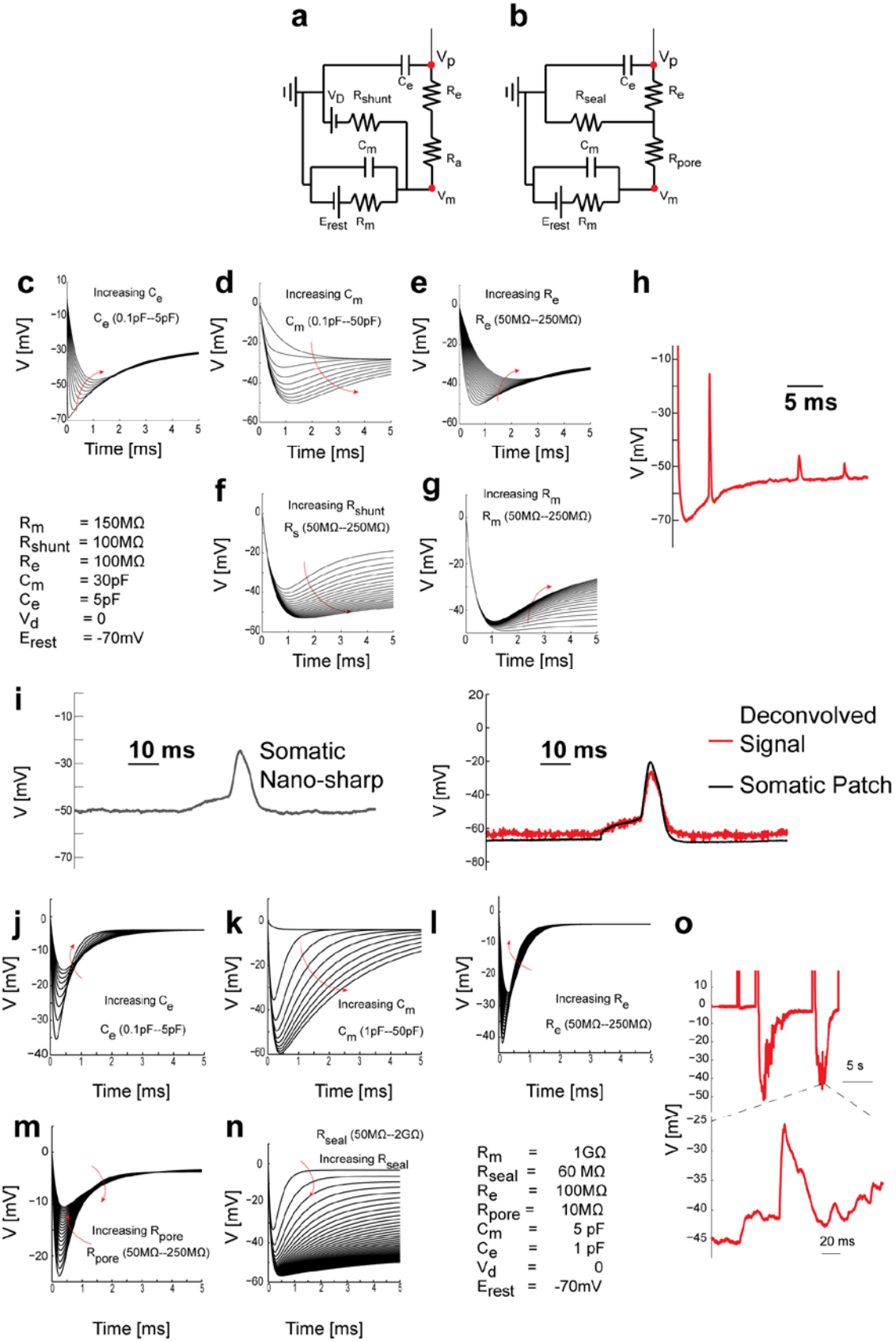

© 2016 Macmillan Publishers Limited, part of Springer Nature. All rights reserved.

Supplementary Figure 3:Equivalent circuit describing the nanopipette membrane interface during **a,** penetration (model-A) and **b,** electroporation based entry (model-B). Here R_e, C_e is the pipette resistance and capacitance respectively. R_a, R_{shunt}, R_{seal} and R_{pore} represents the access resistance, the shunt resistance , the seal resistance and the pore resistance respectively. R_m depicts the membrane resistance, C_m the membrane capacitance and E_{rest} the resting membrane potential respectively. V_d is the diffusion potential between the inside of the membrane and outside which under grounded bath conditions can be approximated to zero. Also, no current flows into the amplifier since it is a high impedance node. **c-g,** transient response of the circuit shown in **(a)** under varying C_e, C_m, R_e, R_{shunt} and R_m. Notice how C_e, C_m and R_{shunt} affect the ability to achieve a stable RMP. **h,** Experimentally observed impalement transient in the soma. Notice the clear trough in the transient which is close to the actual RMP~-70mV. **i,** Measured AP waveform using a nanopipette (left) after impalement based entry. Using the measured time constants, simultaneous somatic patch clamp signal and equation set describing model-A ,the AP waveform was inverse filtered (red curve, right) to reveal the true amplitude. Notice the close temporal match between both waveforms. **j-n,** transient response of the circuit shown in **(b)** under varying C_e, C_m, R_e, R_{seal} and R_{pore}.The R_m is assumed to be very high to mimic the spine head. Notice how R_{seal} and C_m have a profound influence on the ability to achieve a stable RMP. Also, due to the voltage division the RMP nominally achieved is approximately 30-50mV. (o) Experimentally observed electroporation based (model-B) entry into the spine head (two consecutive attempts on the same spine). The RMP is found to quickly drop to -52mV and subsequently discharge. The steady state RMP achieved is very much in line with the transient analysis. Also, notice the EPSP waveform and time scale (inset, zoom) which is in line with our deconvolved EPSP amplitudes (Fig. 5l, main manuscript).

The transient solutions to the equivalent circuits (Eq.1 and Eq. 4a) shown in **Supplementary Fig. 3(a&b)** were solved in Matlab and plotted in **Supplementary Fig. 3(c-g)** and **Supplementary Fig. 3(j-n)**. As observed in **Supplementary Fig. 3(c-g)**, after impalement, the effect of the C_m, C_e and R_{shunt} have the most profound influence on the magnitude of the steady state RMP. A low R_{shunt} (in comparison to R_m), will preclude an accurate estimate of the RMP, even under optimal compensation . Also, cells and structures with small C_m values will be unable to hold the charge for too long and dissipate it through the RC time constant ($R_m C_m$).

© 2016 Macmillan Publishers Limited, part of Springer Nature. All rights reserved.

Thus to record from small C_m structures, R_{shunt} has to be extremely high (approaching several 100'sMΩ and much larger than R_m) to avoid the detrimental effects of shunting. A similar situation occurs with electroporation induced entry. Here, C_m, C_e and R_{seal} have the most pronounced effect on the measured RMP. R_m however, could change during entry. It is important to note that equations (1&4) do not account for changes in R_m due to activation of channels or loading resistors (see section on RMP in spine head for details) but still provide intuition.

- *Deconvolution procedure for APs and EPSPs:*

Using Eq.3 and Eq.4b the scaling factor was calculated from the actual and steady state RMPs measured in each electrode. The observed response was then rescaled using this scaling factor, and inverse filtered using the measured RC time constant of the pipette (see methods). We point out that, in some cases a tip potential formed just prior to or just after nanopipette removal from the membrane and was subtracted from the DC RMP value (nominally~-1-4mV). Moreover, the RC pipette time constant just after entry was established changed by a factor (2-10), i.e. R_e changes by a factor of two to three (80MΩ to approximately 160-240MΩ) either due to tip potential variations, ionic concentration gradients and membrane contact while the wall capacitance changed from 1pF to approximately 2-3pF, possibly due to QD desorption. Inverse filtering was performed by either deconvolving the impulse response ($\frac{1}{R_eC_e}e^{\frac{-t}{R_eC_e}}$) from the measured signal using the Inverse Fourier Transform with appropriate zero padding or using the well known expression[4], $V_{recovered} = V_{observed} + R_eC_e\frac{dV_{observed}}{dt}$, after rescaling . Both methods gave us identical results. The same approach was used, when measuring EPSP amplitudes in the spine head. Since, the actual RMP's (during spontaneous entry under high seal formation; ~-60mV) and the measured DC baseline under electroporation were known, the voltage divider ratio was extracted and EPSP and AP amplitudes in the spine head were scaled.

- *Estimating R_{seal} and R_{pore}:*

© 2016 Macmillan Publishers Limited, part of Springer Nature. All rights reserved.

R_{shunt}, R_{seal} and R_{pore} were first calculated from dual patch-nanopipette recordings in the soma of the neuron. The input resistance of the cell (calculated through hyper-polarizing current pulses), was measured from the patch pipette before and after nanopipette entry. The relationship between the input resistance and the shunt is given by,

$$R_{in2} = \frac{R_{in1} \times R_{shunt}}{R_{in1} + R_{shunt}} \quad \text{or} \quad (5a)$$

$$R_{in2} = \frac{R_{in1} \times R_{(pore+seal)}}{R_{in1} + R_{(pore+seal)}} \quad (5b)$$

depending on the mode of entry (i.e. model A or model B). The effective R_{shunt} was readily known from Eq. 5(a) or Eq. 5(b) once the input resistances were calculated. With model B **(Supplementary Fig. 3(b))** , Eq. 4b was additionally used, to ascertain R_{seal} once $R_{seal}+R_{pore}$ was known from Eq. 5(b), i.e. from the measured steady state RMP's. Using this value of R_{seal}, R_{pore} was then ascertained. The range for R_{shunt} , R_{seal} and R_{pore} extracted were (~500MΩ-800MΩ), (20-120MΩ, mean~65.75MΩ, n=4) and (~144-300MΩ, mean~ 185.48MΩ, n=4) respectively.

- *Estimating* R_{neck} *:*

bAP amplitudes were re-scaled using the extracted voltage divider ratio (i.e. from RMP measurements, Eq.4) . However, we know from dendritic recordings (Fig.4c in main manuscript), spine recordings **Supplementary Fig. 8(c-d)**, and from previous work on voltage indicators[5] that bAP's back-propagate along dendrites and invade the spine with nearly no loss. When we used the extracted voltage division ratio from the RMP's (Eq.4) to estimate the spine head bAP amplitude, we often found that the bAP amplitude was attenuated in comparison to the somatic AP. This occurred because the bAP was now divided across the R_{neck} and R_{pore} (i.e. R_{pore} dominates the effective R_m looking in from the neck, refer Fig. 5a main manuscript). Since we know the expected bAP amplitude from the somatic patch electrode, the attenuated bAP amplitude in the spine head (from Eq.4) and experimental estimates for R_{pore} , we used the following expression (Eq. 6) to extract a plausible range for R_{neck} ,

© 2016 Macmillan Publishers Limited, part of Springer Nature. All rights reserved.

$$V_{bAP\_spinehead} = \frac{V_{bAP} \times R_{pore}}{R_{neck} + R_{pore}} \qquad (6)$$

➢ *The RMP of the spine head during entry:*

Electroporation induced entry (model-B) into spines normally results in the formation of both a significant R_{pore} and moderate R_{seal} (evidenced through RMP measurements). However, and although less frequent, electroporation induced entry ensured a very low R_{pore} and high R_{seal}, resembling a model-A type entry. Such a situation is aptly reflected in **Supplementary Fig. 13** and Fig .5j in the main manuscript, where the RMP's reached ~-30mV to -60mV, albeit for a brief period of time (~100-300ms).

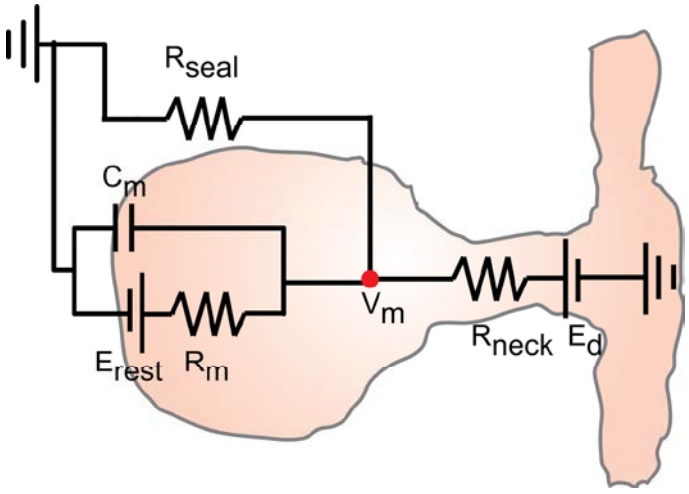

Supplementary Figure 4. The equivalent circuit in the spine head upon pipette penetration. Here R_m, R_{seal}, R_{neck}, C_m and E_{rest} have their usual meanings as described before. E_d is the leak reversal potential in the dendritic shaft. The combination of all circuit elements decide the steady state potential in the spine head.

Using Eq.1 and Eq.4 and realistic spine head properties (R_m ~10's-100s of GΩ, specific resistance (leak) ~5KΩcm^2-20KΩcm^2 [6-7], C_m ~0.01pF) this would seem infeasible. This is because, with moderate R_{seal} values (~100'sMΩ) and exceedingly high R_m (10s-100GΩ), RMP registration of ~-60mV is impossible. We surmise that i) The spine head R_m reduced during entry (possibly due to activation of synaptic conductances) and (ii) the RMP of the spine head, is influenced by the weighted effects of R_{neck} and R_{seal} which act as loading resistors

© 2016 Macmillan Publishers Limited, part of Springer Nature. All rights reserved.

(**Supplementary Fig. 4** and Eq.7). Assuming, R_m ~5GΩ, R_{seal} ~500MΩ, R_{neck} ~500MΩ and $E_m = E_d \approx -70mV$, the spine head RMP upon entry is approximately -35mV (Eq.7), which is in line with the results shown in **Supplementary Fig. 13**. Together, Eq.6 and our recordings indicate that upon entry, the effective R_m of the spine head reduces to approximately ~1-5GΩ. Similar values of R_m have been reported for mossy fiber boutons (diameter~4um) through giga-seal patch-clamp recordings[8].

$$V_m = \frac{E_{rest}R_{seal}R_{neck} + E_d R_m R_{seal}}{R_{seal}R_m + R_{seal}R_{neck} + R_m R_{neck}} = V_{e\_steady\_state} \quad (7)$$

© 2016 Macmillan Publishers Limited, part of Springer Nature. All rights reserved.

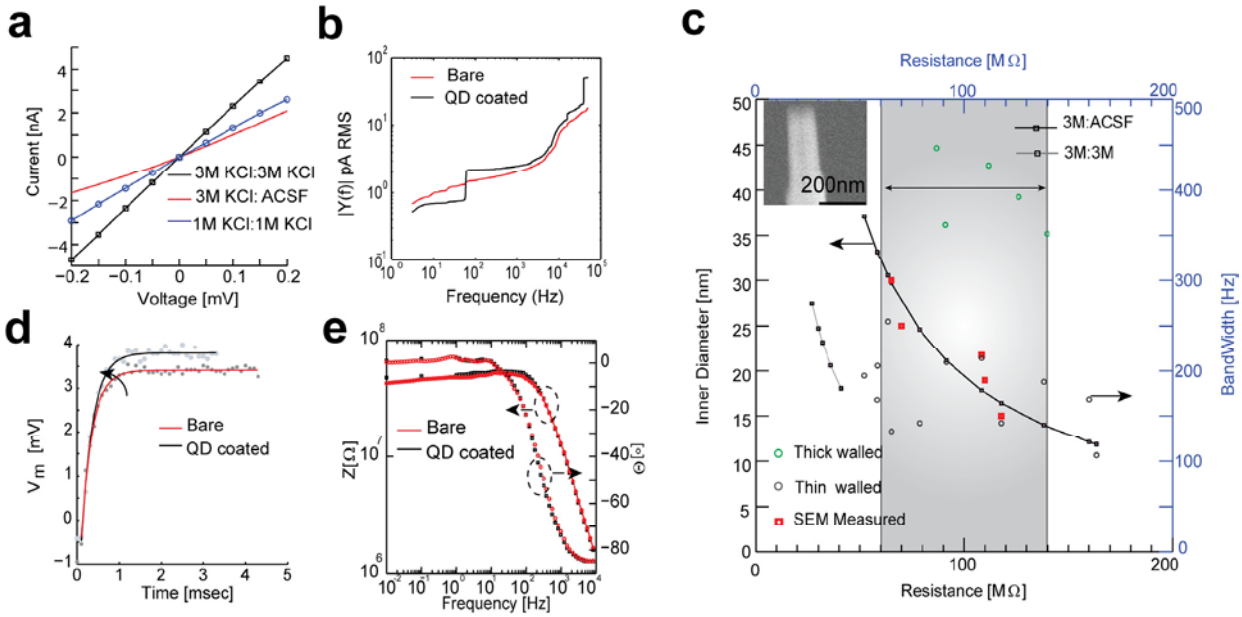

Supplementary Figure 5. Nanopipette characterization a, I-V response of the nanopipette with and without concentration gradients across the tip. The filling solution comprised 3M KCl while the extracellular bath was varied from 3M KCl to ACSF (~120mM NaCl) **b,** current noise for both bare and QD treated nanopipettes in the presence of a concentration gradient across the tip. QD coatings did not impact the integrated (amplifier bandwidth 40KHz) noise. **c,** analytically calculated nanopipette inner-diameters , both in the presence and absence of a concentration gradient (left axis, see methods in main manuscript for equation details) was in agreement with SEM measured diameters (n=5, red squares). Note that when a concentration gradient is established the conductivity at the tip changes which translates the curve along the x-axis. The shaded region depicts the range of pipette resistances used. The uncompensated 3-dB bandwidth vs. measured resistance (right axis) depicts a nominal bandwidth of ~200Hz (grey dots). Using thicker pipettes, increased the bandwidth to ~400Hz (green dots). **d,** The 3-dB bandwidth was calculated by fitting the pipettes voltage response to a current pulse and corroborated through **e,** impedance spectroscopy. See methods in main manuscript for model and method details.

© 2016 Macmillan Publishers Limited, part of Springer Nature. All rights reserved.

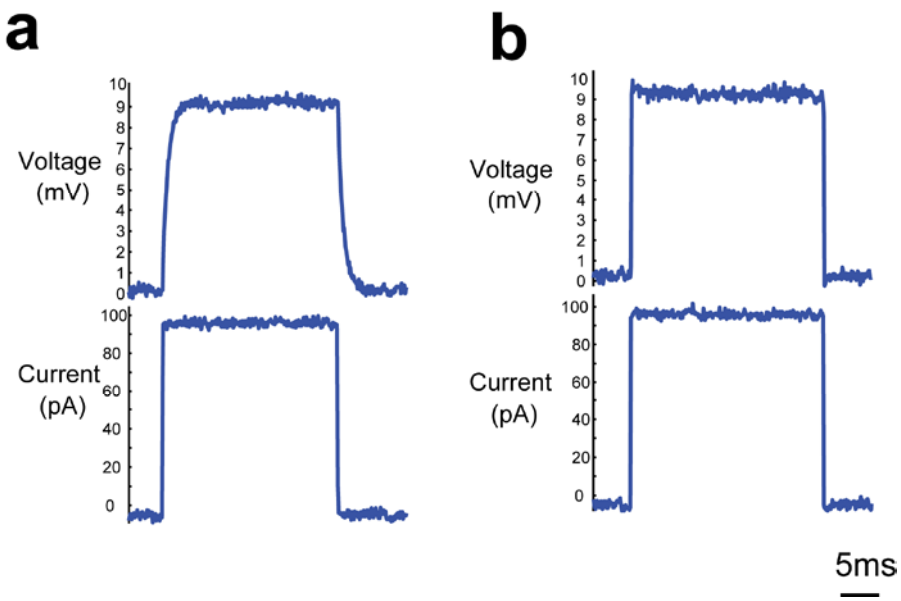

Supplementary Figure 6. Nanopipette capacitance compensation. Voltage response of the nanopipette (upper trace) to current injection (lower trace) before (**a**) and after (**b**) capacitance compensation. Notice the sharp rising and falling edges after compensation has been applied.

© 2016 Macmillan Publishers Limited, part of Springer Nature. All rights reserved.

Supplementary Note 3: Effect of electroporation and duration of spine recordings

In order to demonstrate whether and to what extent nanopipette penetration and electroporation create permanent intracellular physiological changes, we first performed simultaneous nanopipette and Ca^{2+} imaging measurements in dendrites and subsequently in spine heads.

➢ *Electroporation and its effect on Dendrite physiology*

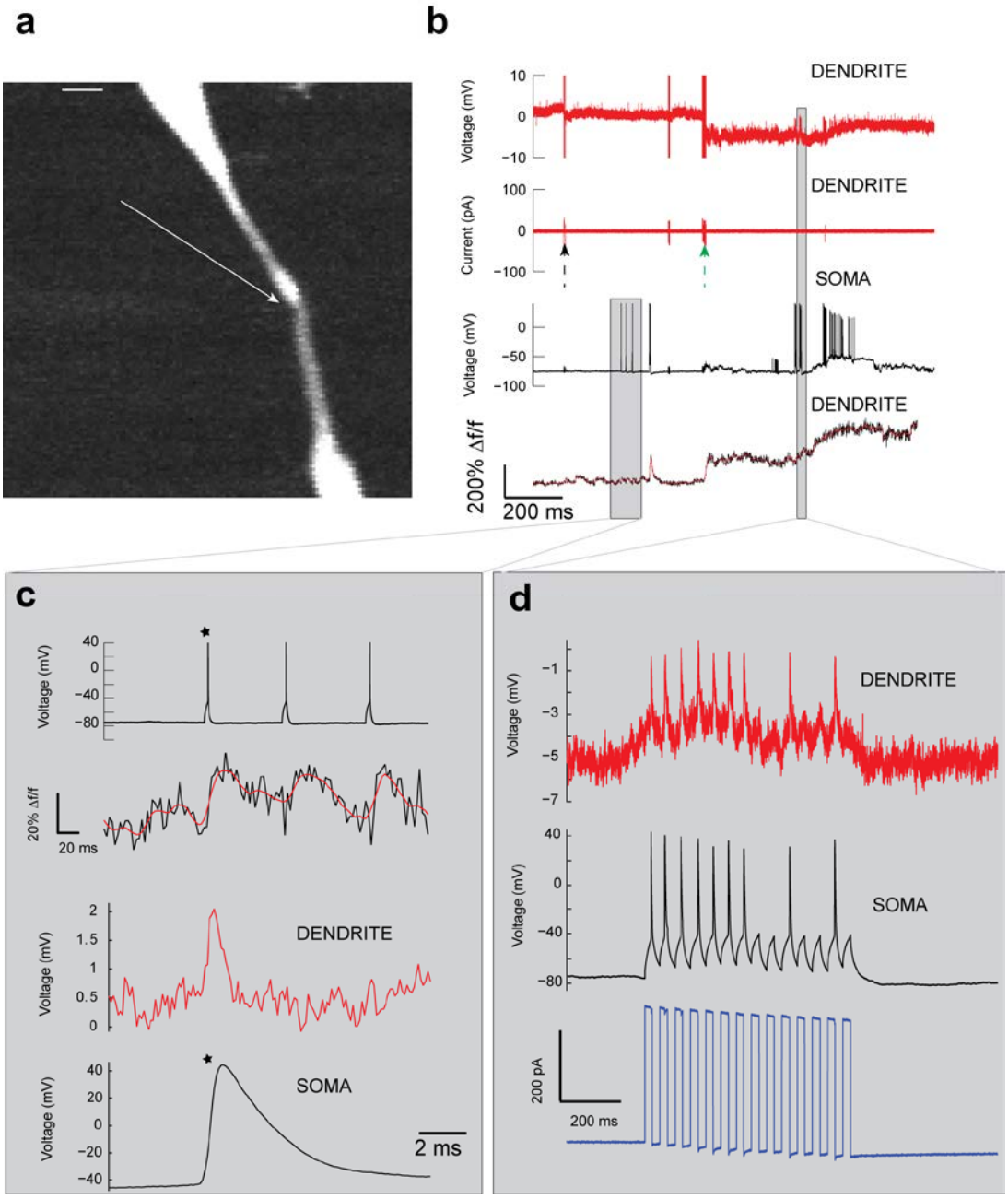

© 2016 Macmillan Publishers Limited, part of Springer Nature. All rights reserved.

Supplementary Figure 7. **Dendritic electrophysiology and calcium imaging**. **a,** Two-photon image of the nanopipette in contact with the apical dendrite (white arrow) (scale bar, 3 μm). The neuron was loaded with Alexa-594 and a Ca^{2+} indicator (Fluo-4). **b,** simultaneous nanopipette recordings in the dendrite (marked red; first row depicts voltage; second row depicts current), somatic patch recordings (black; third row) and Ca^{2+} imaging in the proximal apical dendrite (red and black; last row; red trace represents a smooth function over 100 frames). Upon nanopipette contact with the dendrite, a weak electroporation pulse (i.e. "touch and buzz" with a short duration electroporation pulse application; black dotted arrow; second row) was applied followed by mechanical advancement and a strong electroporation pulse (i.e. buzz with either longer pulses or increased frequency of stimulation; green dotted arrow; second row). bAPs elicited through somatic current injection were clearly observed in the Ca^{2+} trace both before and after the application of the strong electroporation pulse. **c,** Single bAPs elicited right after the first weak electroporation cycle, resulted in concomitant Ca^{2+} signals (second row) and nanopipette recordings (third row; signal corresponds to somatic AP marked by a star in the first row) in the dendrite. Notice that the RMP in the dendritic recording is not yet negative, which indicates a very high pore resistance (model B in the main manuscript). The AP waveform however, resembles the intracellular AP elicited through somatic current injection, which suggests a tight seal recording. **d,** Dendritic voltage and Ca^{2+} signals following mechanical advancement and application of a strong electroporation pulse (green dotted arrow in **b**; second row). bAPs were clearly observed in the dendritic recordings (red; first row) with higher SNR and a negative steady state potential. Notice that although the soma was slightly depolarized (evidenced by the RMP becoming more positive) and there was an increase in baseline fluorescence (last row in **b**), the characteristics of the APs including sub-threshold depolarization's were detectable in the dendrite.

As shown above in **Supplementary Fig. 7(a)**, the cell was loaded with Fluo-4 and Alexa-594 through the somatic patch (see methods in main manuscript). A position approximately 50um from soma, along the main apical dendrite was identified, and the nanopipette was advanced to this location. We recorded the concomitant somatic and dendritic electrophysiological properties, and, simultaneously monitored the Ca^{2+} signals in the dendrite (frame rate: 15Hz, **Supplementary Fig. 7(b)**). We then applied a weak buzz (50us) followed by a strong buzz (100us) through the nanopipette (indicated by the black and green dotted arrows in the second trace in **Supplementary Fig. 7(b)**). Right after the application of the first weak buzz, somatic action potentials were triggered using the patch electrode and were observed both electrically in the nanopipette channel and in the fluorescent channel **(Supplementary Fig. 7(c))** respectively.

© 2016 Macmillan Publishers Limited, part of Springer Nature. All rights reserved.

The bAP detected by the nanopipette in **Supplementary Fig. 7(c)** clearly indicates that the nanopipette formed a tight seal recording with the dendrite, but did not achieve full penetration, although, the waveform resembled an intracellular spike. This highly filtered intracellular like action potential waveform suggests the presence of a very tiny pore. In stark contrast, when we applied a strong buzz through the nanopipette (to create a lower pore resistance), we noticed a depolarization in the soma as well. This was most probably due to the creation of a larger hole which also allowed more Ca^{2+} to flow in thereby increasing the fluorescent signal (reflected by the increase in baseline in **Supplementary Fig. 7(b)**). The electrophysiological properties of the soma and dendrite however, even after the creation of such a pore were not affected and bAPs triggered at the soma were observed in the dendrite without loss in temporal sensitivity (**Supplementary Fig. 7(d)**). Sub-threshold depolarization transients caused by current injection that did not result in an action potential were also clearly observed. This result clearly suggests that the pore created during electroporation, if too large, will preclude functional Ca^{2+} measurements. This however, may not be as detrimental to the electrophysiological signals (relative amplitude and time scale), and could still provide adequate information on local voltage build up. In order to prolong the duration of recordings and enable physiologically balanced amounts of ion exchange between the inside and outside of the membranes under study, the electroporation induced pore needs to very small.

© 2016 Macmillan Publishers Limited, part of Springer Nature. All rights reserved.

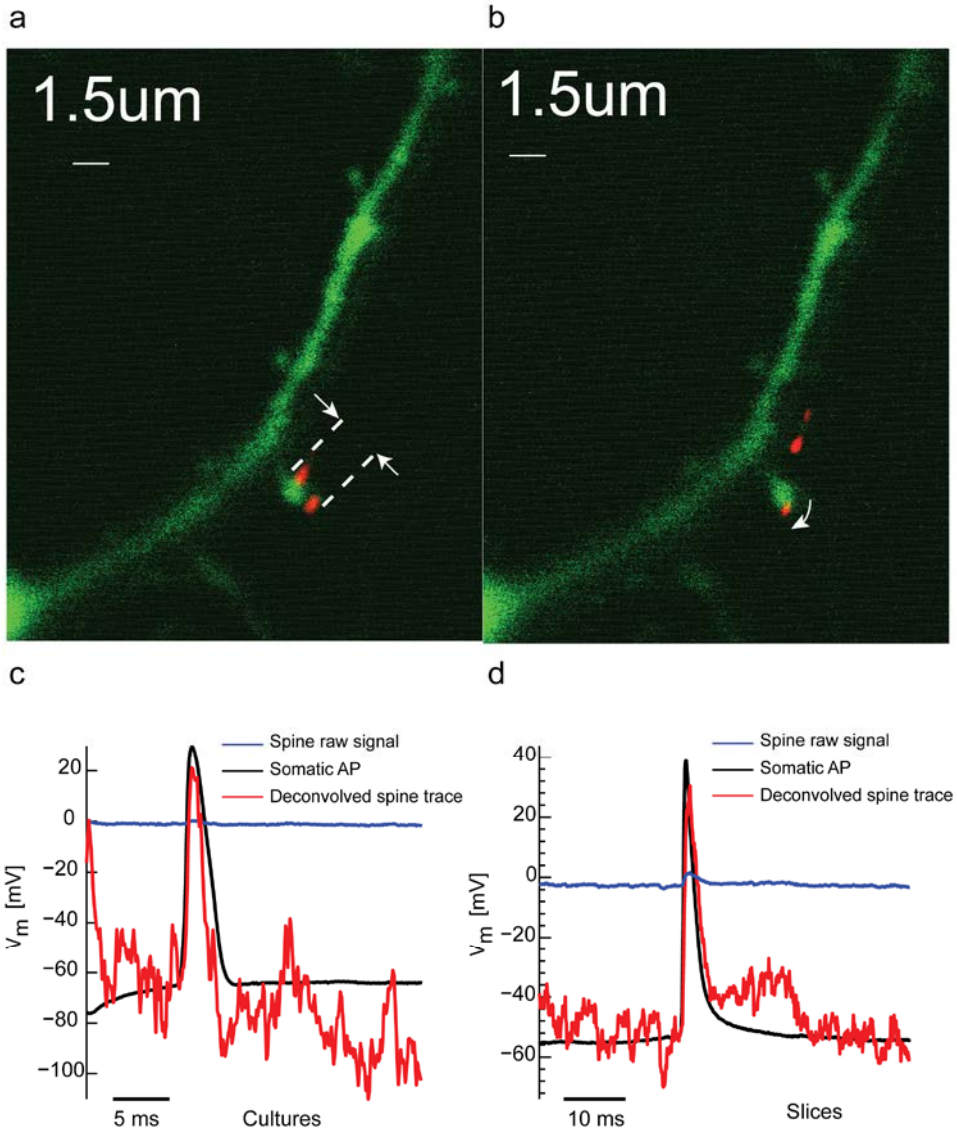

Supplementary Figure 8. Nanopipette spine coupling: a, Interaction between the nanopipette and the spine (from Fig.5b in manuscript). The nanopipette was steered between the two white lines during spine head entry, notice QD desorption from the pipette (lower spot), **b,** After the pipette is withdrawn, desorbed QD's were found to move with the spine head. Inverse filtering bAP amplitudes from spines in **c,** cultures and **d,** slices reveals full invasion with nearly no loss. Raw signal represents a single trial without averaging.

- *Electroporation and its effect on SPINE physiology*

In order to assess if electroporation affects the physiology of dendritic spines when attempting to gain intracellular access to the spine head, we performed two distinct sets of experiments

© 2016 Macmillan Publishers Limited, part of Springer Nature. All rights reserved.

(**Supplementary Fig. 9&10**). In the first experiment (**Supplementary Fig. 9(a-d)**) we initially stimulated the spine through electroporation (E-field stimulation which results in a 1V, 100ms pulse inside the pipette) while simultaneously monitoring the electrophysiological signals in the spine head and soma, and, Ca^{2+} signals in the spine head and dendritic shaft respectively (frame rate 15Hz). The nanopipette was in contact with the spine head but not mechanically advanced to penetrate the membrane. We clearly observed spontaneous post-synaptic potentials in the spine head during the application of the electroporation pulse (**Supplementary Fig. 9(b&c)).** The Ca^{2+} signals in the spine did not show a response during this period. Subsequently, after the loss of signal from the spine head (possibly due to recovery of the pore) (indicated by green arrows in **Supplementary Fig. 9(b)**), we triggered bAPs from the soma which were registered in the spine head Ca^{2+} trace. This showed that the spine head was physiologically intact, was not damaged during the initial nanopipette entry and recovered after the nanopipette broke out. In **Supplementary Fig. 9(d)**, we depict three stages post electroporation via heat maps (which indicate fluorescence) to elucidate its effect on both the spine head and dendritic shaft physiology; the figure denotes the average Ca^{2+} response (~33 seconds (i.e. 500 frames)) (i) just after the application of the electroporation pulse on the spine head (denoted by black dotted lines in **Supplementary Fig. 9(a);** fourth row; marked (i)), (ii) during the application of somatic current injection resulting in bAPs invading the spine head and dendritic shaft respectively (denoted by blue dotted lines in **Supplementary Fig. 9(a);** fourth row; marked (ii)) and (iii) after both mechanical and electroporation induced entry (denoted by green dotted lines in **Supplementary Fig. 9(a);** fourth row; marked (iii)). As expected, mechanical penetration followed by electroporation resulted in a severe depolarization in the spine head which eventually led to a large Ca^{2+} signal in the dendrite (region (iii)). The results presented in **Supplementary Fig. 9(a&d)** suggest that mechanical penetration followed by stimulation to the spine head, results in large amounts of Ca^{2+} influx into the spine, while weak electroporation is not detrimental to the overall physiology of the spine. We do however state that it is still unclear as to whether Ca^{2+} entry affects the local voltage signals in the spine head which could primarily arise due to transport of Na^{+} and K^{+} ions.

© 2016 Macmillan Publishers Limited, part of Springer Nature. All rights reserved.

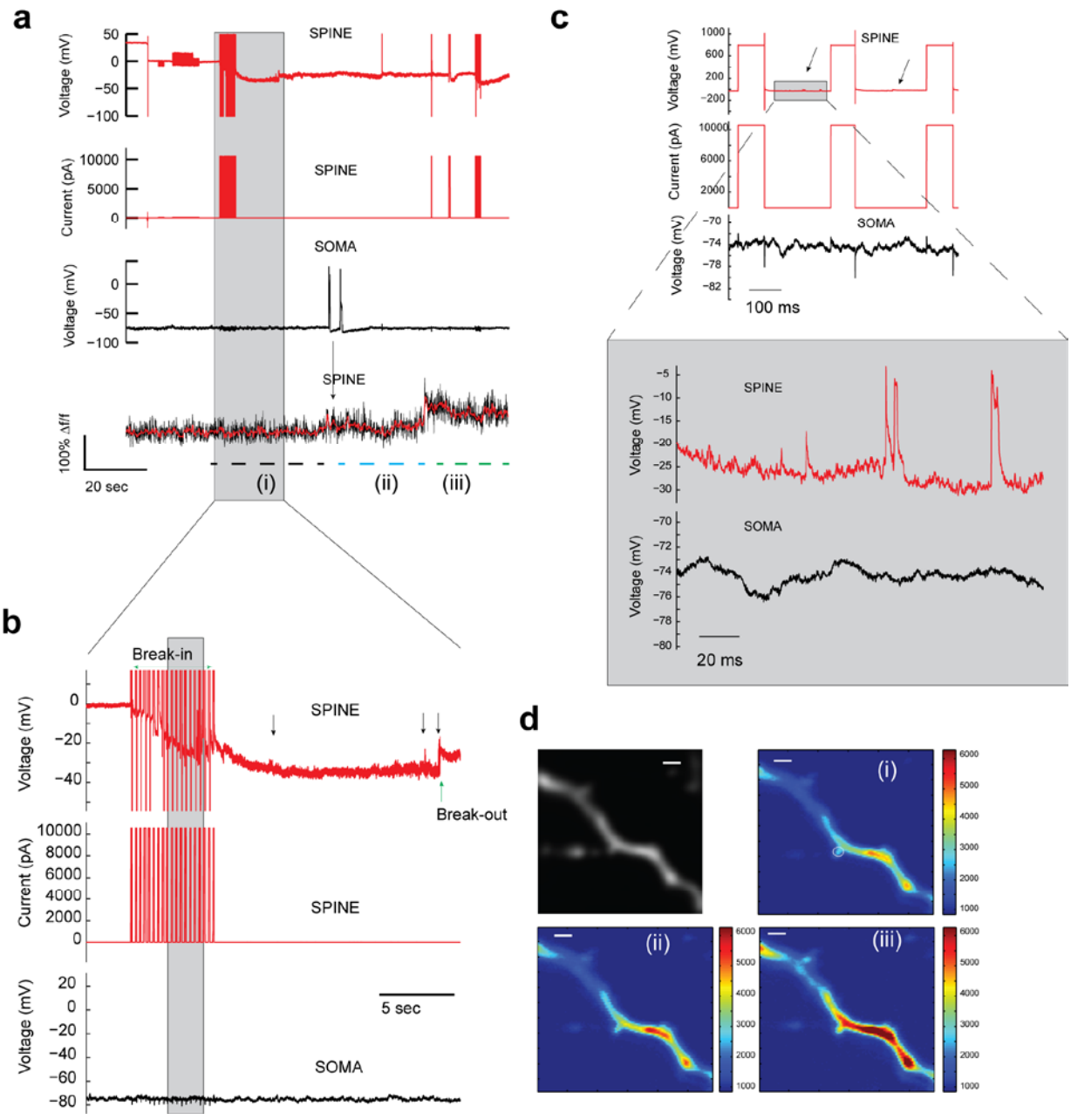

Supplementary Figure 9. **Spine electrophysiology and calcium imaging**. Simultaneous electrophysiology and Ca^{2+} imaging in the spine head shows the spine head is physiologically intact after pipette entry and exist. **a,** Nanopipette voltage recordings in the spine head (marked red; first row) shows break-in and subsequent break-out (shaded region and magnified view in (**b**); marked region (i)) after the application of a strong electroporation pulse (red; second row). Somatic current induced back-propagating action potentials (bAP) (black; third row) clearly shows a Ca^{2+} signal in the spine head (black and red; fourth row; indicated by an arrow; marked region (ii); red curve represents the smoothing over 100

© 2016 Macmillan Publishers Limited, part of Springer Nature. All rights reserved.

frames; frame rate: 15Hz). Mechanical penetration followed by the application of an electroporation pulse, resulted in a much higher spine head Ca^{2+} signal, which, did not recover, but, did not result in a somatic depolarization (marked region (iii)). **b,** magnified view of the region shaded grey in (**a**). The black arrows indicate locations where spontaneous PSPs were observed. The green arrows indicate break-in and break-out of the spine head. **c,** A typical electroporation pulse cycle representative of the regions marked grey in (**b**) (top; black arrows indicate spontaneous PSPs observed) and magnified view of select PSPs in-between individual pulses (bottom; shaded box). Notice that the soma is relatively silent when spontaneous PSPs were observed. Break-out occurs within a few hundred milli-seconds (red; first row). **d**, Two-photon image of the nanopipette spine interaction (upper left corner); heat maps depicting the fluorescence signals at different times during the recording (marked (i)-(iii) in panel (**a**) fourth row; average of 500 frames). (i) Period during, and, just after the application of the electroporation pulse. Notice that the spine head and dendritic shaft Ca^{2+} signal is not high; (ii) period during which, bAP trains were elicited. Notice the slightly increased Ca^{2+} signals in the dendrite but the spine head signal is still low. (iii) Period during which mechanical penetration was followed by the application of electroporation pulses. Notice the large increase in baseline Ca^{2+} fluorescence in the spine head and dendritic shaft respectively. The units of the heat map are arbitrary and represent raw fluorescence levels, (scale bar, 2 μm).

In an alternate experiment (**Supplementary Fig. 10(a)**) and similar to the previous case, we first applied a weak electroporation pulse with the nanopipette in tight contact with the spine head, and, subsequently injected current in the soma to initiate bAPs. The main difference in this experiment was that the nanopipette spine seal was maintained for a longer period of time which allowed for simultaneous recording of voltage and Ca^{2+} signals in the spine head. As shown in the grey shaded region (marked 1) in **Supplementary Fig. 10(a)**, current injection in the soma resulted in bAPs which were registered in the spine head both by the nanopipette and via Ca^{2+} imaging. The size and measured baseline of the spine head voltage indicated a tight seal recording (model B in the main manuscript) with the formation of a tiny pore which precludes a large trans-membrane Ca^{2+} leakage. When we attempted to increase the size of the pore by applying a barrage of electroporation pulses (green dotted lines) and without mechanical stimulation, we noticed a corresponding decrease in the RMP being measured, consistent with a lower pore access resistance. Upon close inspection (shaded region marked no.2) we clearly observed spontaneous post-synaptic potentials (raw signals shown in box marked no.2 below).

© 2016 Macmillan Publishers Limited, part of Springer Nature. All rights reserved.

The panel of images shown in **Supplementary Fig. 10(b)** depicts the nanopipette spine interaction and the Ca^{2+} signals in the spine after the application of electroporation and entry protocols.

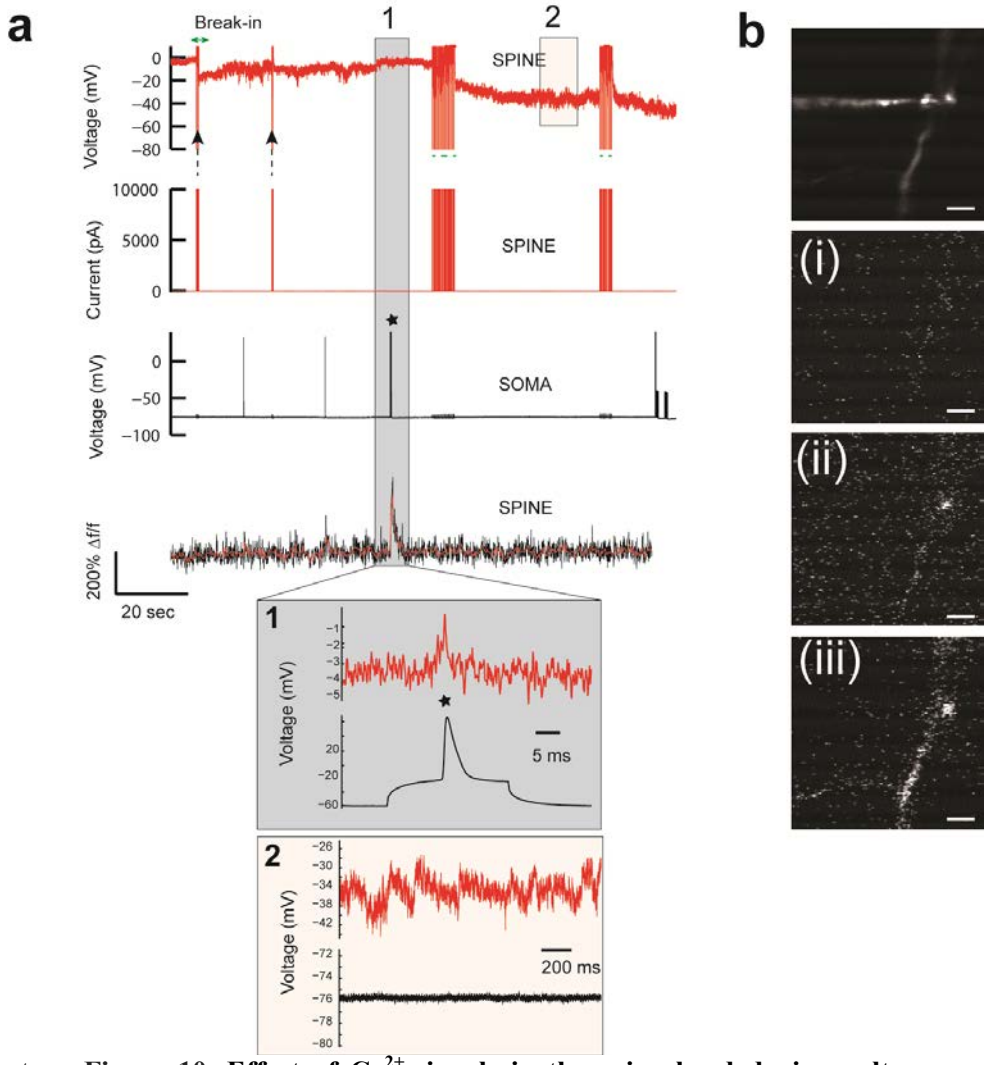

Supplementary Figure 10. Effect of Ca^{2+} signals in the spine head during voltage recording. **a,** Nanopipette recordings of spine head voltage while simultaneously monitoring Ca^{2+} signals with different electroporation pulse protocols. After the application of a weak electroporation pulse (black dotted arrows in row 1), bAPs elicited through somatic current injection were clearly observed both in the Ca^{2+} trace (row 4) and the nanopipette respectively (grey shaded region marked 1; box labeled 1). After the application of a strong (longer duration) electroporation pulse (green dotted lines in row 1), the RMP was found to become more negative with the observation of spontaneous PSPs in the nanopipette trace (cream shaded region; box marked 2). **b,** top panel shows the nanopipette spine interface, specific to the results presented in **(a).** Panel labeled (i) shows the overall Ca^{2+} signal in the spine head and dendrite after the

© 2016 Macmillan Publishers Limited, part of Springer Nature. All rights reserved.

pipette was withdrawn following the experiment outlined in **(a)**. Subsequently the nanopipette was brought back in contact with the spine head and a strong electroporation pulse was applied (panel (ii)). Notice the increase in spine head Ca^{2+} signals alone. Mechanical poking in addition to strong electroporation caused the entire spine head and dendritic shaft Ca^{2+} signal to increase (panel (iii)). Panels (i-iii) represent single frames, (scale bar, 2 μm).

Specifically, **Supplementary Fig. 10(b)** (top) depicts a two photon image of the nanopipette in contact with the spine head. The panel labeled (i) depicts the Ca^{2+} signals in the spine and dendritic shaft after the nanopipette was withdrawn slightly following the experiment outlined in **Supplementary Fig. 10(a)**. Notice that the spine head Ca^{2+} signal is near baseline. Panel (ii) depicts the spine head Ca^{2+} signal upon longer duration electroporation pulses and subsequent nanopipette withdrawal. Notice that only the spine head is affected, evidenced through the higher Ca^{2+} signal while the dendrite is not affected. The panel labeled (iii) depicts the condition after both mechanical penetration and strong electroporation application. Under this condition we observed that both the spine head and dendrite exhibited an extremely high baseline Ca^{2+} signal, indicative of a large trans-membrane Ca^{2+} flux caused during nanopipette entry. Together the results presented in **Supplementary Figs. (7,9&10)** suggest that electroporation induced entry does not drastically affect the physiology of the spine head and dendrites. However, strong repeated electroporation and mechanical penetration can result in a significant membrane shunt resistance (see main manuscript for details) which affects the Ca^{2+} signals in such structures, but, does not appear to have a detrimental effect on the electrophysiology over short durations. Since a majority of our spine head recordings last several hundred milli-seconds to seconds (described next; **see Supplementary Fig. 11**), and given that our entry is based on an electroporation protocol that does not cause long term damage, it is unlikely that the voltage in such structures are affected by trans-membrane ion fluxes during entry.

- *On the duration of recordings from spines:*

In this study, we established two modes of nanopipette entry into the membrane, a) Impalement and b) electroporation based. Impalement based entry resulted in an associated shunt/weak seal resistance which, given the size of the spine, precluded extended duration of recordings (lasting a maximum of ~100ms). With electroporation induced entry however, duration of recordings

© 2016 Macmillan Publishers Limited, part of Springer Nature. All rights reserved.

varied from a ~100ms to several seconds. Measured potentials were however, scaled, which we attributed to the voltage division across the high access resistance of the pore. Under such an entry procedure we often observed a sudden change in RMP, evidenced by a trough in the measured potential followed by a fast recovery to a stable resting state, often very close to the initial baseline value **(Supplementary Fig. 11 (a&b))**. The access resistance of the pore could further change due to recovery of the pore. However, due to the close proximity and tight seal between the nanopipette tip and membrane (**Supplementary Fig. 11(a,c&d))**, the nanopipette was able to register voltage transients with high SNR. It is important to note that after establishing such an entry, we were able to record for durations lasting several hundred milli-seconds to several seconds **(Supplementary Fig. 11(a,c&d))**. Importantly, during the initial break-in to the spine we did not notice a severe depolarization in the soma, which is indicative of probing a compartment that is isolated. Similar entry procedures into dendrites often caused an initial depolarization that was detected in the soma, which indicates the low resistive electrotonic coupling. However, in all cases we did encounter a sudden loss in recording, evidenced through the RMP rapidly reducing, possibly due to excessive shunting and/or loss of seal/contact between the pipette and membrane.

In situations where the pipette tip formed a very stable seal with the spine head **(Supplementary Fig. 11(c))**, we registered bAPs (**Supplementary Fig. 11(c)**, bottom) in the spine with the waveforms resembling extracellular recordings. The RMP however (steady state) reached ~-70mV. This condition is electrically similar to a cell attached (giga-seal) current clamp recording[9]. Under such a condition if the seal resistance is much higher than the patch/pore resistance (i.e. the membrane is still sealed) , the steady state potential measured by the pipette is very close to the actual RMP, while, APs are low pass filtered due to the RC time constant of the membrane -pipette interface. EPSPs on the other hand were also observed although, filtered and smaller in magnitude than those observed through actual intracellular access. The exact mechanism on how such a tight seal is created still nebulous, and could depend on the microscopic interaction between the membrane and pipette tip. Specifically, micro-scale membrane folding around the tip could occur, effectively sealing the tip[10]. However, such a seal allowed recordings lasting hundreds of seconds. If such a condition could be engineered more often, it would allow much longer experiments without the loss of seal. This can potentially be achieved through the use coatings containing lipid layers[11].

© 2016 Macmillan Publishers Limited, part of Springer Nature. All rights reserved.

In **Supplementary Fig. 11(d)** we report a spine recording that lasted several seconds. Here electroporation induced entry into a spine caused an initial depolarization in the soma which recovered to a stable baseline. EPSP waveforms in the spine were clearly observed even ~60s after gaining entry with raw waveforms depicting 15-30mV amplitudes. The downstream somatic EPSP was relatively silent (~0.5mV flickers), which was consistent with earlier results.

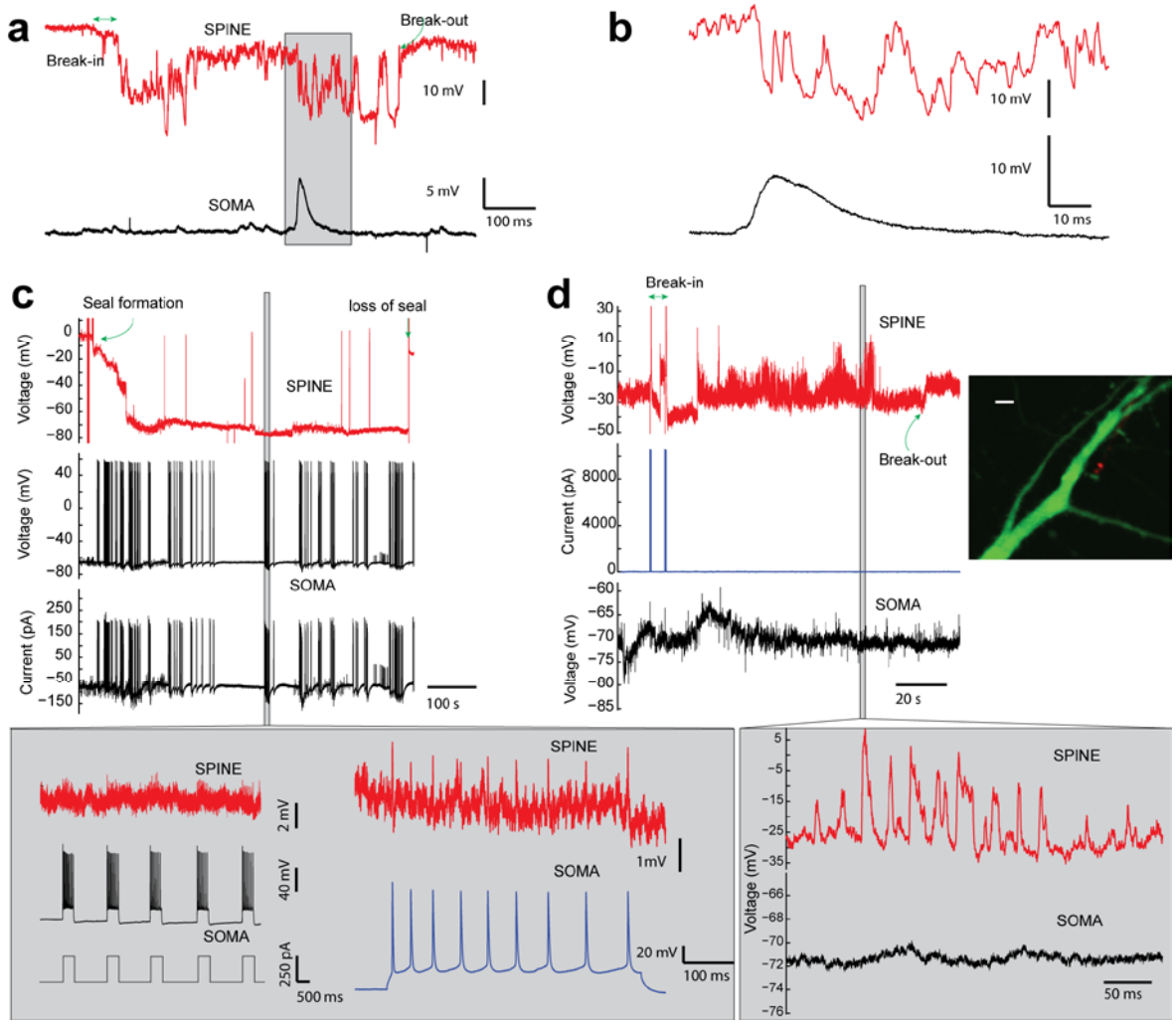

Supplementary Figure. 11. **Varying durations of nanopipette recordings in the spine head**. **a,** Application of simultaneous mechanical advancement and electroporation, causes break-in into the spine head (raw data; top) which lasts a few hundred milli-seconds. The corresponding somatic trace (bottom) is shown below. **b,** zoomed in plot of the area shaded grey in **a**. The spontaneous potentials in the spine head recording although noisy, do show potential fluctuations with milli-second rise and decay times. **c,** Simultaneous spine head and somatic patch recording in which the nanopipette formed an extremely high

© 2016 Macmillan Publishers Limited, part of Springer Nature. All rights reserved.

seal but did not gain complete intracellular access. Notice the clear registration of bAPs in the spine head (shaded region; panel shaded grey) albeit exhibiting extracellular characteristic. The duration of recordings in this case could last upto a few hundred seconds, but such an interface condition precludes the measurement of fast transients and small potentials. **d,** Weak electroporation induced break-in to the spine head allows intracellular access which allows for the clear registration of spontaneous PSPs (raw data; lower panel shaded grey). Break-out (loss of recording) occurs within 60 seconds. Notice the fast rise and decay kinetics of the PSPs. Inset: nanopipette in contact with the spine head (scale bar, 2 μm).

While nanopipette recordings in the soma could last an hour and more and the longest dendritic recordings typically between 15-30 minutes (with electroporation induced entry and re-entry), we were not able to achieve the same duration of recordings in spines (several hundred milliseconds to several seconds). We however, stress that the durations reported in this study were long enough to estimate with high temporal sensitivity, the spontaneous potentials that originated in the spine head.

© 2016 Macmillan Publishers Limited, part of Springer Nature. All rights reserved.

Supplementary Note 4:

➢ *On the rise and decay of Dendritic Spine EPSPs*

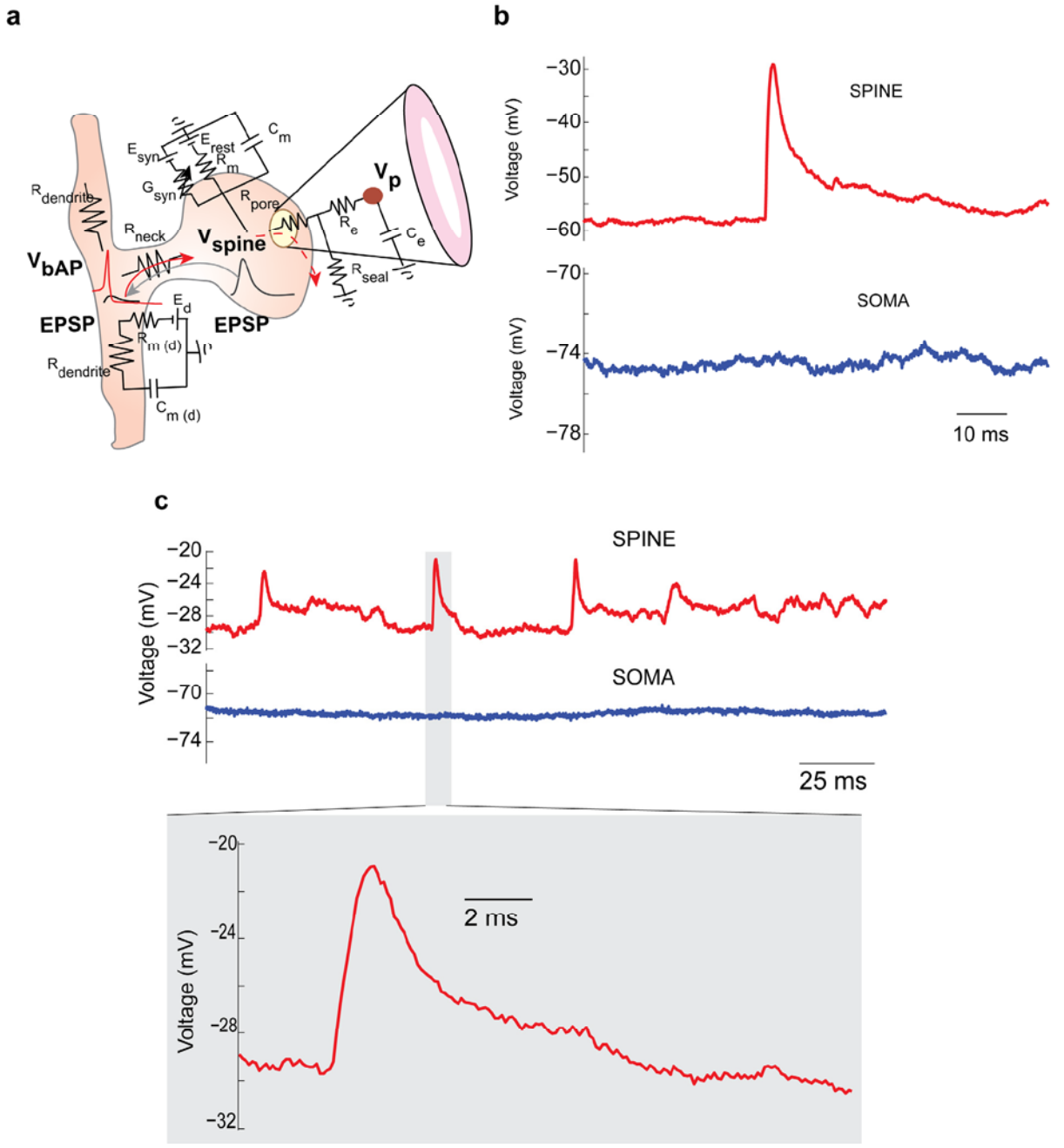

Supplementary Figure. 12. Rise and decay characteristics of EPSP waveforms. a, Electrical equivalent circuit of the passive dendritic spine. E_{rest}, leak reversal potential; R_m, spine head passive membrane resistance; C_m, spine head passive membrane capacitance; E_{syn}, synaptic reversal potential;

© 2016 Macmillan Publishers Limited, part of Springer Nature. All rights reserved.

g_{syn}, synaptic conductance; R_{pore}, pore resistance; R_{seal}, seal resistance; R_{neck}, neck resistance; R_e, pipette resistance; C_e, pipette capacitance; $R_{dendrite}$, dendritic resistance; $R_{m(d)}$, dendrite passive membrane resistance; $C_{m(d)}$, dendrite passive membrane capacitance; E_d, dendrite reversal potential. **b-c**, Typical rise and decay kinetics for spontaneous PSPs recorded in the spine head. Notice the milli-second resolution rise and decay indicative of an extremely small RC time constant. The data shown in **b,c** is not deconvolved.

We observed fast rising EPSPs in the spine head (1ms-3ms) with typical decay times that range between 10ms -50ms (**Supplementary Fig. 12**). We explain this feature based on the following model[12]. The displacement of voltage in the dendritic spine depends not only on the magnitude and shape of the synaptic current entering the spine but also on the passive membrane properties of the spine head and neck. The voltage in the spine head thus depends on both the characteristics of the synaptic branch and passive membrane properties (G_{syn}, E_{syn} and $g_{rest} = 1/R_m, C_m$) (see **Supplementary Fig. 12(a)** for circuit). Following the established analysis of post-synaptic potential generation outlined by Segev[12], we solve for membrane voltage when the net current across the membrane is zero (Eq.8) (i.e. when no external current is injected across the membrane) and the special case in which the synaptic input is a rectangular pulse of amplitude G_{syn} and duration t_{syn}.

$$C_m \frac{dV_m}{dt} + g_{rest} V_m + G_{syn}(t)(V_m - E_{syn}) = 0 \qquad (8)$$

i.e. $I_C + I_{rest} + I_{syn} = 0$

Here I_C, I_{rest} and I_{syn} represent the capacitive, resting channel and synaptic current respectively. The solution $V_m(t)$ obtained by separation of variables and integration (Eq. 9) describes the build-up in membrane voltage when channels are opened with the steady state solution given by Eq. 10.

$$V_m(t) = \frac{G_{syn}}{G_{syn} + g_{rest}} E_{syn}\left(1 - e^{-t\frac{(G_{syn}+g_{rest})}{C_m}}\right) \text{ for } (0 \le t \le t_{syn}) \qquad (9)$$

The steady state solution, obtained when the synaptic channels are opened for an infinitely long duration $(t_{syn} \to \infty)$ is given by:

© 2016 Macmillan Publishers Limited, part of Springer Nature. All rights reserved.

$$V_m(t) = \frac{G_{syn}}{G_{syn} + g_{rest}} E_{syn} = \frac{1}{1 + \frac{g_{rest}}{G_{syn}}} E_{syn} \qquad (10)$$

As observed from Eq.9, the time constant is dependent on both the synaptic and resting membrane conductances, which along with the extremely small capacitance of the spine head, results in a small time constant. This causes the EPSP to exhibit a fast and sharp rising phase. The decay is based solely on $g_{rest} = 1/R_m$ (assuming G_{syn} is absent) and could vary depending on the change in g_{rest}. This results in a longer EPSP decay. It is also clearly observed from Eq.10 that the relationship between $V_m(t)$ and E_{syn} is non-linear which would result in a non-monotonic rise/decay in voltage with multiple successive inputs impinging on the same spine. What is clear from the above analysis is that, $EPSP_{spine\_head}$ is dependent on the passive and active properties of the spine head membrane. Additionally, in the event of a low G_{syn}, $EPSP_{spine\_head}$ is dependent on the effective sum of R_{neck} and $R_{dendrite}$ as well (Eq. 1 in the main manuscript). The dendritic or somatic EPSP however, is ($EPSP_{soma/dendrite}$) (assuming electrotonically connected) dependent on the passive membrane properties of the dendritic branch given by Eq.11 below (Eq. 11 is a modification to Eq. 2 from the main manuscript). Equation 11 indicates that a fast ac component in the EPSP signal (rise and decay) will be heavily filtered (due to the overall dendritic capacitance) while slow signals (i.e. dc and low frequency components) will be more affected by the resistive divider (between the neck and dendrite).

$$EPSP_{soma/dendrite} = EPSP_{spine\_head} \frac{Z_{dendrite}}{R_{neck} + Z_{dendrite}} \qquad (11)$$

© 2016 Macmillan Publishers Limited, part of Springer Nature. All rights reserved.

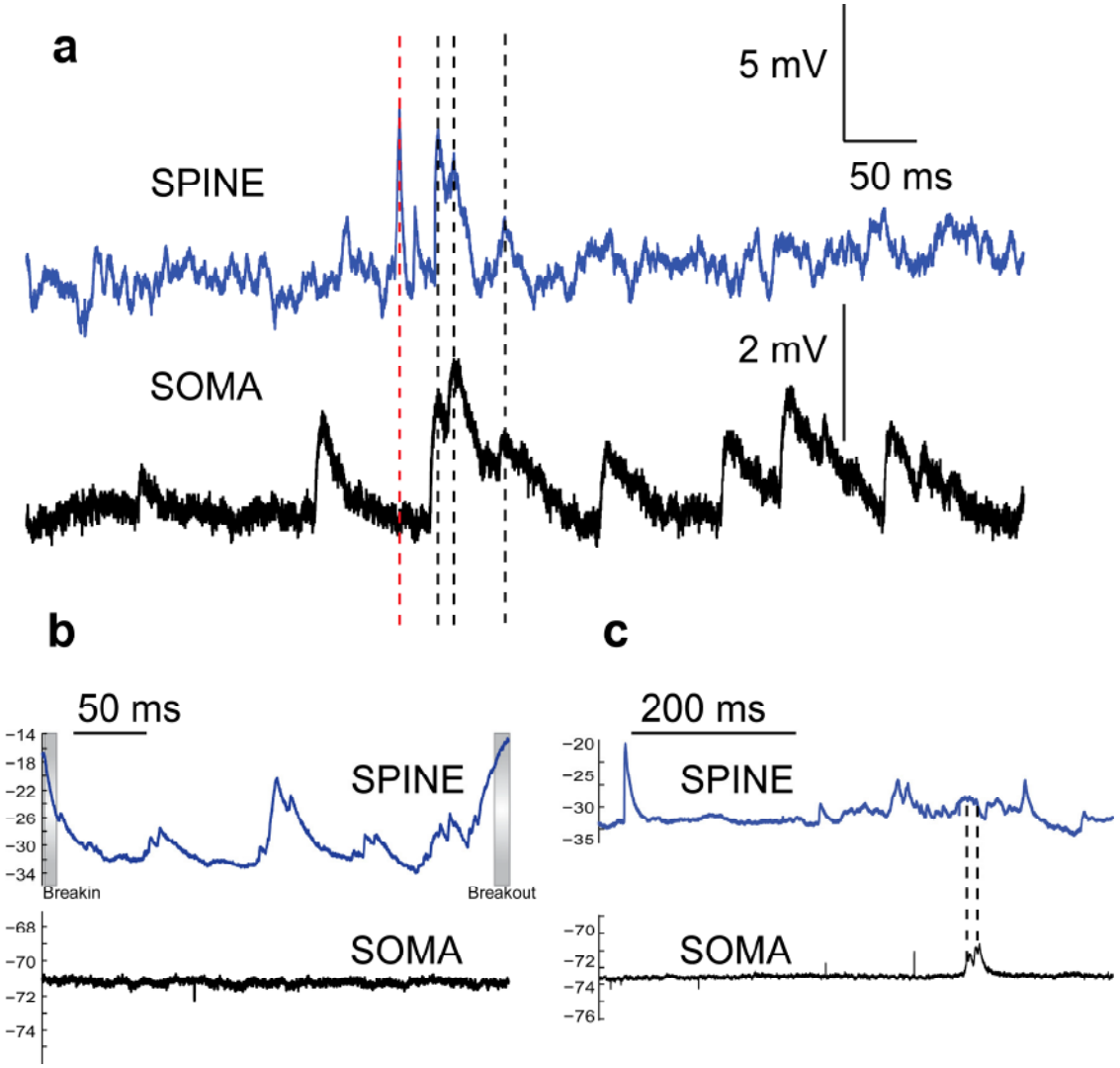

Supplementary Figure 13. simultaneous somatic and spine EPSPs ***a****, EPSP coupling between the spine head and soma (from Fig.5k in manuscript). The three black dotted lines reflect peak to peak registry in both the somatic and spine recordings. The red dotted line signifies EPSPs observed only in the spine head but not in the soma (**b**) A prototypical example of momentary break-in into the spine head and subsequent break-out. Observe that while EPSP's in the spine head are clearly registered, the soma is relatively silent. (**c**) Another example of spine head EPSP's sporadically coupling to the soma, Notice the large (un-scaled) EPSP amplitudes in the spine head in comparison to the somatic EPSP amplitudes. The black dotted lines denote peak-plateau registry in both channels.*

- *Possible reasons for time locked registration of somatic and spine potentials*

As observed in figure 5k in the main manuscript and **Supplementary Fig. 13** above, there appears to be an occasional somatic EPSP that is detected along with the spine head potential. So what is

© 2016 Macmillan Publishers Limited, part of Springer Nature. All rights reserved.

the reason for this occasional time locked registration and is the recorded somatic EPSP truly from the recorded spine ? There could be two possible scenarios through which this could occur : a) active electrical regulation of the spine R_{neck} [13-15], leading to a modulation in the degree of compartmentalization or b) simultaneous co-active inputs from other spines, which integrate to increase the somatic EPSP. The spine head EPSP in the latter case could add to the overall summation or remain completely isolated. It is interesting to note that the amplitude of the spine head EPSPs were similar across the duration of recordings (marked by stars in Fig.5k in main manuscript) and did not change appreciably when concomitant EPSPs in the soma were registered (Fig. 5k, main manuscript, bottom), which could occur if R_{neck} changed (see Eq.1 in main manuscript). Although, this need not occur if the G_{syn} is extremely large. Furthermore, the time locked somatic EPSP amplitudes (~1.5-2mV) were lower in comparison to the raw spine head EPSP (~30mV when deconvolved) which rules out voltage invasion into the spine from other inputs as the source of the signal. Although, we do not have direct evidence to rule out R_{neck} regulation as a mechanism, it is unlikely to occur over the time scales of the EPSPs observed. Previous reports have reported on physical contractions of the neck which lead to differences in synaptic strength[16], however this was shown to occur over the time course of seconds. We thus rule out regulation of R_{neck} as the cause for time-locked registration of EPSPs observed, suggesting instead, that simultaneous co-active inputs are the reason for time locked registration of EPSPs.

© 2016 Macmillan Publishers Limited, part of Springer Nature. All rights reserved.

References

1 Peng, Z. A. & Peng, X. Formation of high-quality CdTe, CdSe, and CdS nanocrystals using CdO as precursor. *Journal of the American Chemical Society* **123**, 183-184 (2001).

2 Hendricks, M. P., Campos, M. P., Cleveland, G. T., Jen-La Plante, I. & Owen, J. S. A tunable library of substituted thiourea precursors to metal sulfide nanocrystals. *Science* **348**, 1226-1230 (2015).

3 Ince, C. *et al.* Intracellular microelectrode measurements in small cells evaluated with the patch clamp technique. *Biophysical journal* **50**, 1203-1209 (1986).

4 Richardson, M. J. & Silberberg, G. Measurement and analysis of postsynaptic potentials using a novel voltage-deconvolution method. *Journal of neurophysiology* **99**, 1020-1031 (2008).

5 Acker, C. D., Yan, P. & Loew, L. M. Single-voxel recording of voltage transients in dendritic spines. *Biophysical journal* **101**, L11-L13 (2011).

6 Chiu, C. Q. *et al.* Compartmentalization of GABAergic inhibition by dendritic spines. *Science* **340**, 759-762 (2013).

7 Popovic, M. A., Gao, X., Carnevale, N. T. & Zecevic, D. Cortical Dendritic Spine Heads Are Not Electrically Isolated by the Spine Neck from Membrane Potential Signals in Parent Dendrites. *Cerebral Cortex* (2012).

8 Geiger, J. R. & Jonas, P. Dynamic control of presynaptic Ca 2+ inflow by fast-inactivating K+ channels in hippocampal mossy fiber boutons. *Neuron* **28**, 927-939 (2000).

9 Perkins, K. L. Cell-attached voltage-clamp and current-clamp recording and stimulation techniques in brain slices. *Journal of Neuroscience Methods* **154**, 1-18 (2006).

10 Angle, M. R., Cui, B. & Melosh, N. A. Nanotechnology and neurophysiology. *Current opinion in neurobiology* **32**, 132-140 (2015).

11 Fu, T.-M. *et al.* Sub-10-nm intracellular bioelectronic probes from nanowire–nanotube heterostructures. *Proceedings of the National Academy of Sciences* **111**, 1259-1264 (2014).

12 Segev, I. in *The Book of GENESIS: Exploring Realistic Neural Models with the GEneral NEural SImulation System* 79-96 (Springer New York, 1998).

13 Bloodgood, B. L. & Sabatini, B. L. Neuronal activity regulates diffusion across the neck of dendritic spines. *Science* **310**, 866-869 (2005).

14 Grunditz, Å., Holbro, N., Tian, L., Zuo, Y. & Oertner, T. G. Spine Neck Plasticity Controls Postsynaptic Calcium Signals through Electrical Compartmentalization. *The Journal of Neuroscience* **28**, 13457-13466 (2008).

15 Perkel, D. H. & Perkel, D. J. Dendritic spines: role of active membrane in modulating synaptic efficacy. *Brain research* **325**, 331-335 (1985).

16 Araya, R., Vogels, T. P. & Yuste, R. Activity-dependent dendritic spine neck changes are correlated with synaptic strength. *Proceedings of the National Academy of Sciences* **111**, 2895-2904 (2014).

© 2016 Macmillan Publishers Limited, part of Springer Nature. All rights reserved.